Multi-scale investigation of the effect of photocurable polyethylene glycol diacrylate (PEGDA) on the self-assembly of cellulose nanocrystals (CNCs)

Lorenzo Metilli, Samuel Mandin, Ioanna Chazapi, Erwan Paineau, William Chèvremont, Nicolas Hengl, Frédéric Pignon, Bruno Jean

Journal of Colloid and Interface Science 685 (2025) 476–486

Contents lists available at ScienceDirect

Journal of Colloid And Interface Science

journal homepage: www.elsevier.com/locate/jcis

Regular Article

Multi-scale investigation of the effect of photocurable polyethylene glycol diacrylate (PEGDA) on the self-assembly of cellulose nanocrystals (CNCs)

Lorenzo Metilli [a,b,*], Samuel Mandin [b], Ioanna Chazapi [c], Erwan Paineau [c], William Chèvremont [d], Nicolas Hengl [b], Frédéric Pignon [b], Bruno Jean [a]

[a] Université Grenoble Alpes, CNRS, CERMAV, 601 Rue de la Chimie, Gières, 38610, France
[b] Université Grenoble Alpes, CNRS, Grenoble INP, Laboratoire Rhéologie et Procédés, 363 Rue de la Chimie, Gières, 38610, France
[c] Université Paris Saclay, CNRS, Laboratoire de Physique des Solides, 1 rue Nicolas Appert, 91405, Orsay, France
[d] ESRF, The European Synchrotron, 71 Avenue des Martyrs, Grenoble, 38043, France

GRAPHICAL ABSTRACT

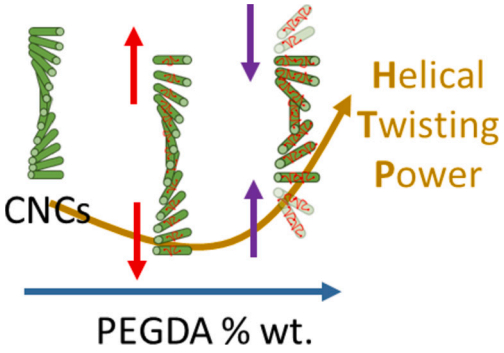

ARTICLE INFO

https://doi.org/10.15151/ESRF-ES-1553323761

Keywords:
Cellulose nanocrystals
Self-assembly
Small-angle scattering
Polymers
Rheology

ABSTRACT

Cellulose nanocrystals (CNCs) are appealing building blocks to replace plastic for the fabrication of more sustainable photonic and barrier materials. Aqueous suspensions of CNCs are typically mixed with polymers to improve the mechanical flexibility of the dry nanocomposite, adding further functionalities. However, the role of the additives in the suspension state, and how they affect the processing and final properties of the material still requires further studies. In this work, the interactions between CNCs and polyethylene glycol diacrylate (PEGDA), a water-soluble, photocurable polymer, were investigated through a multi-scale approach involving small-angle X-ray and light scattering (SAXS and SALS). PEGDA was found to adsorb on the surface of CNCs, exhibiting two behaviour regimes depending on the mass ratio between PEGDA and CNCs (R_{PC}). Below a threshold ratio ($R_{PC} = 0.5$), PEGDA weakened the chiral interactions between CNCs, reducing the anisotropic volume fraction and increasing the cholesteric pitch. Above this threshold ($R_{PC} > 0.5$), the adsorbed polymer enhanced the helical twisting power, resulting in higher amounts of anisotropic phase and shorter pitch values. This non-monotonic trend was attributed to the structure of the adsorbed PEGDA layer on the surface of the CNCs, first masking the chiral features of the twisted nanoparticles, then enhancing the transmission of chirality due to changes in particle morphology and effective particle volume fraction. A simultaneous decrease in the suspension dielectric constant amplified this effect, strengthening interparticle interactions. Finally, rheo-optical experiments provided

* Corresponding author at: Université Grenoble Alpes, CNRS, CERMAV, 601 Rue de la Chimie, Gières, 38610, France.
E-mail addresses: lorenzo.metilli@cnrs.fr (L. Metilli), bruno.jean@cermav.cnrs.fr (B. Jean).

https://doi.org/10.1016/j.jcis.2025.01.155
Received 12 November 2024; Received in revised form 16 January 2025; Accepted 18 January 2025
Available online 20 January 2025

further insights into the formation of the cholesteric structure, showing that larger amounts of polymer delayed the isotropic-cholesteric phase transition.

1. Introduction

Driven by ever-increasing environmental concerns, research on biopolymers has gained momentum over the last decades, attempting to replace petroleum-based materials with more sustainable alternatives [1]. Cellulose, the most abundant biopolymer on earth, is available in the form of nanofibres or nanocrystals by mechanical and/or chemical processing of sources such as wood, tunicates, and bacteria, among others. These building blocks, in turn, can be processed into self-standing, biocompatible materials, such as films, membranes, gels and porous scaffolds for valuable applications [2].

Cellulose nanocrystals (CNCs) are compelling starting materials, owing to their high tensile strength (7.7 GPa), low density (1.6 gcm^{-3}), large surface area and ease of chemical modification. CNCs are rod-like, crystalline particles typically obtained from the acid hydrolysis of cellulose microfibrils. The acid treatment decorates their surfaces with sulfate half-ester groups, which in turn endow CNCs with colloidal stability in both aqueous and in some non-aqueous media (DMSO, DMF) [3]. CNCs exhibit liquid crystal behaviour in polar and non-polar solvents, self-assembling and separating into a chiral nematic phase and an isotropic phase. The chiral nematic, or cholesteric organisation, can be described as a series of pseudoinfinite planes of CNCs aligned in the same direction, which turn in a helicoidal fashion around the axis perpendicular to the CNCs' planes. The period of the helix, termed cholesteric pitch, falls in the micrometre range for aqueous suspensions of CNCs [4].

The cholesteric structure is maintained upon removing the solvent, allowing the production of CNC-based thin films with attractive photonic properties. Typically, the cholesteric pitch is reduced to few hundreds of nanometres, interacting with visible light and giving rise to the so-called "structural colours" [5]. Moreover, the structural organisation of CNCs can be modulated by modifying the properties of the particles and suspensions (*i.e.*, size and surface chemistry, concentration, ionic strength), as well as by applying external stimuli, such as shear flow and electromagnetic radiation, increasing the versatility of CNC-based materials [6]. The processing of CNC suspensions into films, carried out by increasing the concentration through controlled solvent removal, is hindered by several drawbacks that limit its industrial deployment [5]. These include structural heterogeneities caused by concentration gradients during evaporation, and the brittleness of the film due to the crystalline nature of CNCs, both compromising the functionality and flexibility of the final material [7].

To overcome these limitations, polymers are often added to CNC suspensions, acting as plasticizers in the dry nanocomposite. Polyethylene glycol diacrylate (PEGDA) is a hydrophilic and biocompatible PEG derivative capped by two acrylate moieties, which can cross-link under UV radiation in presence of a suitable initiator molecule. Over the last decade, the combination of PEGDA and CNCs to develop new materials has been reported in the literature. Examples include the preparation of CNC-PEGDA hydrogels and their processing via 3D-printing into scaffolds for tissue engineering [8–11], or stimuli-responsive CNC photonic films, prepared from solvent casting and evaporation [12–14]. More recently, PEGDA was used to prepare oriented thin film nanocomposites by combining ultrafiltration of CNCs with subsequent photocuring [15].

In all cases, the physicochemical interactions between PEGDA and CNCs are critical to the properties of the suspension, and therefore towards the processability of said suspensions into the final materials. However, few of the cited articles have led an investigation in this regard. Huang et al. (2020) and Feng et al. (2023) conducted FT-IR studies on the nanocomposites containing CNC and cross-linked PEGDA, reporting the presence of hydrogen bonding between the two components [13,12]. Nonetheless, the adsorption of the more common species PEG on CNCs in the suspension state is still being debated in the literature [16,17], and a systematic study concerning the PEGDA derivative in the liquid and solid state is missing. This gap of knowledge is due to the complex multi-scale behaviour exhibited by CNC suspensions, and the necessity of a suitable investigation approach to link all the relevant lengthscales (nanometre to micrometre).

This work attempts to fill this gap by investigating the physicochemical interactions between PEGDA and CNCs in aqueous suspensions. First, the interactions between nanoparticles and polymer were studied in diluted conditions, aiming at highlighting adsorption phenomena on the surface of the CNCs. Then, the effect of adding PEGDA on the liquid crystalline behaviour of CNCs was examined, combining the use of small-angle scattering techniques to assess changes of the structural behaviour at the nanoscale and microscale. Finally, rheometry coupled with optical microscopy was employed to analyse the CNC and PEGDA suspensions, linking the evolution of flow properties to the appearance and the size of the cholesteric domains.

2. Materials and methods

2.1. Materials

Cellulose nanocrystals (CNCs) were purchased from UMaine Development Centre (University of Maine, USA) as an aqueous suspension in their Na^+ form (10.6% wt.), with a sulphur content of 1.1 g per 100 g of CNCs [18]. The CNCs were dispersed by sonication using a Branson Digital Sonifier (Emerson Electric Company, USA), with a sonication dose of 130 $kJ{\cdot}g^{-1}{\cdot}L^{-1}$. The dose was calculated by first determining the acoustic power of the apparatus under set operating conditions (30% duty cycle, 100% power output) on a 10.6% wt. CNC suspension, as described by Taurozzi et al. (2011) [19]. Then, the dose was normalized by the sonication time, the suspension volume and concentration of CNCs, following recent guidelines in the literature [20,21]. The dimensions of the CNCs were previously determined using electron microscopy and image analysis [22]. The CNCs were 127.4 ± 34 nm in length, and 10.9 ± 2.6 nm in width.

Polyethylene glycol diacrylate (PEGDA, molecular weight 675-725 $g{\cdot}mol^{-1}$, average molecular weight 700 $g{\cdot}mol^{-1}$) was purchased from Sigma Aldrich (Sigma Aldrich, France) and used without further purification. The samples were prepared by adding PEGDA to the CNC suspension, leaving them under magnetic mixing for 24 h prior to analysis. The ionic strength of the samples was controlled by diluting the concentrated CNC aqueous suspension with a NaCl solution (10 mM). These samples were labelled according to the mass ratio between PEGDA and CNCs, using the nomenclature $R_{PC} = x$.

Another set of samples was prepared by varying simultaneously the amount of CNCs and PEGDA. In this case, the nomenclature for the samples was C*X*P*Y*, where X and Y represent the mass fraction of CNCs and PEGDA, respectively. The ionic strength varied between 0.22 mM and 1 mM.

2.2. Isothermal titration calorimetry (ITC)

The interactions between CNCs and PEGDA molecules were investigated using a Nano ITC instrument (TA Instruments, USA). The CNC suspension (0.1% wt.) was titrated using a 0.1% wt. PEGDA solution, in aliquots of 10 μL. Additional experiments were carried out by varying the concentration of CNCs (0.05, 0.5, 1% wt.). For each experiment, 22 injections were performed every 500 s at 25 °C under constant stirring (300 rpm). The heat of CNC-PEGDA interaction was normalized

by subtracting the heat of dilution of PEGDA, CNC and water with distilled water. The resulting data were processed with the NanoAnalyze software (TA Instruments, USA).

2.3. Quartz crystal microbalance with dissipation monitoring (QCM-D)

The experiments were carried out using a Q-Sense E4 instrument (Biolin Scientific, Sweden). The adsorption of PEGDA on CNCs was carried out by first injecting a solution of polyetherimine (PEI) (0.1% wt.), on a gold disc, which was previously cleaned using an ultrasonic bath. The flow rate was set to 50 $\mu L \cdot min^{-1}$ throughout the experiment. The cell was rinsed with a buffer solution (10 mM NaCl), waiting until the measured fundamental resonance frequency and dissipation energy stabilized. Then, the CNC and PEGDA solutions (0.1 and 1% wt., respectively) were injected in sequence into the cell. The variations in the resonance frequency and dissipation were measured also for the 3rd, 5th, 7th and 11th overtones.

2.4. Dynamic light scattering (DLS) and electrophoretic mobility (EM)

The apparent particle size and electrophoretic mobility of CNCs as a function of PEGDA content were determined using a Malvern Zetasizer ZS (Malvern Panalytical, United Kingdom). The particle concentration was diluted to 0.1% wt. with a 1 mM NaCl solution, and the cell temperature set to 25 °C. The measurements were carried out in 15 cycles for the particle size (10 for the electrophoretic mobility), in triplicates.

2.5. Fourier transform infrared spectroscopy (FT-IR)

Fourier-transform spectra were acquired using a Spectrum Two instrument (Perkin Elmer, USA), equipped with a liquid cell. The samples were placed between two CaF_2 windows, using a 20 μm Teflon spacer. The spectra were collected between 4000 and 1000 cm^{-1}, using a 4 cm^{-1} resolution, with a total of four scans per sample.

2.6. Small-angle X-ray scattering (SAXS)

A first set of SAXS measurements was carried out at the SWING beamline (SOLEIL, Saint-Aubin, France). The incident energy was fixed at 16 keV ($\lambda = 0.048$ nm), with a beam size of 75x375 μm^2. The scattering patterns were collected on an Eiger 4M photon-counting X-Ray detector (Dectris, Switzerland) placed in the vacuum tunnel of the beamline at two distances (6.2 and 0.5 m), with a resulting scattering vector (q) range of $1.4 \cdot 10^{-2}$ to $2.5 \cdot 10^{1}$ nm^{-1}. Prior to the experiments, the samples were placed in borosilicate capillaries that were flame-sealed and stored vertically. Data reduction of the scattering patterns was obtained using the FOXTROT program available on the beamline.

The second set of SAXS measurements was performed at the TRUSAXS instrument (beamline ID02) (ESRF, Grenoble, France) on quartz capillaries containing the C*XPY* samples. The incident energy was 12.23 keV ($\lambda = 0.101$ nm), beam size 50x25 μm^2 and the sample-to-detector distance (SDD) set to 10 m, with a scattering vector q from 0.007 to 0.7 nm^{-1}. The interparticle distance between CNCs (d_{CNC}) was calculated from the peak of the azimuthally-averaged 1D intensity using Eq (1):

$$d_{CNC} = 2\pi / q^{*} \quad (1)$$

where q^* is the wavevector corresponding to the position of the peak. For both datasets, background and solvent signals were subtracted from the scattering patterns, returning the absolute scattering intensity I(q) (mm^{-1}).

2.7. Small-angle light scattering (SALS)

SALS measurements were performed using a bespoke setup previously reported in the literature [23,24]. The samples were poured into 2 mm quartz cuvettes (Hellma Analytics, Germany), sealed with Parafilm, and stored in the dark for 7 days. The cuvettes were illuminated with a He-Ne laser (λ = 632.5 nm), and the scattered intensity was focused with a Fresnel lens towards the detector (AV MAKO G-419B POE CMOS sensor, Allied Vision). The recorded 2D scattering patterns was regrouped and averaged with a custom MATLAB-based software (Mathworks, USA) and SAXSutilities2, respectively [25,26]. The q range provided by the SALS setup was between $2.3 \cdot 10^{-5}$ and $7 \cdot 10^{-3}$ nm^{-1}. The cholesteric pitch (P) was calculated from the first-order peak intensity of the 1D azimuthally-averaged scattering patterns, according to Eq (2):

$$P = 4\pi / q^{**} \quad (2)$$

where q^{**} is the wavevector corresponding to the position of the peak.

2.8. Polarized photography

The anisotropic volume fraction of the samples was calculated by taking photographs of the sealed cuvettes (Hellma Analytics, Germany) using two cross-polarizers to enhance the contrast due to the birefringence of the anisotropic phase. The volume fraction was calculated by measuring the ratio of the total suspension height and the height of the anisotropic phase with ImageJ software (National Institute of Health, USA).

2.9. Polarized light microscopy (PLM)

The samples were sealed between a microscope slide, an adhesive spacer of height = 250 μm and a coverslip, and let to rest vertically in the dark for 7 days. Images were taken with a Leica DM LM polarized light microscope (Leica, Germany), using a magnification of 20x and 50x. The cholesteric pitch P was calculated from the Fourier transform images of the fingerprint pattern, using a custom image processing workflow developed in Python. For each sample, 10 images were collected and analysed, and the average pitch value calculated.

2.10. Rheometry and rheo-microscopy

Rheological measurements were carried out on a Physica MCR 501 stress-controlled rheometer (Anton Paar, Austria). The samples were sheared between 0.01 and 1000 s^{-1} using a cone-and-plane measuring system (75 mm diameter, 149 μm truncation height, angle 0.991°). The measurements were carried out in triplicates at 20 °C, using a solvent trap to prevent solvent evaporation.

Measurements were also carried out in oscillation mode, using a glass cone-and-plane measuring system (50 mm diameter, 55 μm truncation gap, angle 0.991°). The samples were first subject to an oscillation step for 5 minutes (1% amplitude, 1 Hz), followed by 1 minute of shear at 1000 s^{-1} and an oscillation step (1% amplitude, 1 Hz) for 60 minutes. Polarized microscopy images were acquired throughout the experiment every 15 seconds using the Rheo-microscope accessory to monitor the microstructure of the samples. The cholesteric pitch was determined using the same image analysis workflow as for the PLM images.

3. Results and discussion

3.1. Molecular interactions between CNCs and PEGDA

The physiochemical interactions between CNCs and PEGDA were first assessed by ITC (Fig. 1). Upon injecting the PEGDA solution in the ITC cell, a series of endothermic peaks were observed. The normalized heat, obtained by subtracting the contribution of water, CNCs and PEGDA (Supporting Information Figure S1) in Fig. 1, reached a plateau at $R_{PC} = 0.1$; the signal was attributed to the adsorption of PEGDA molecules onto the surface of CNCs present in the ITC cell. Additional experiments with more dilute CNC concentrations, set to detect the onset of the sigmoidal curve typically observed in ITC experiments, are

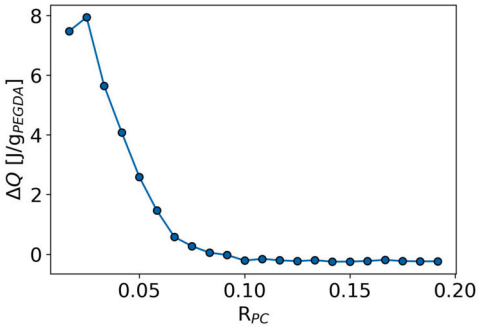

Fig. 1. Isothermal titration calorimetry (ITC) experiment, showing the normalized heat obtained by subtracting the contribution of water-water, water-CNCs and water-PEGDA dilution, as a function of the mass ratio between PEGDA and CNC (R_{PC}). The CNC suspension (0.1% wt.) was titrated with a 0.1% wt. PEGDA solution in 10 μL aliquots.

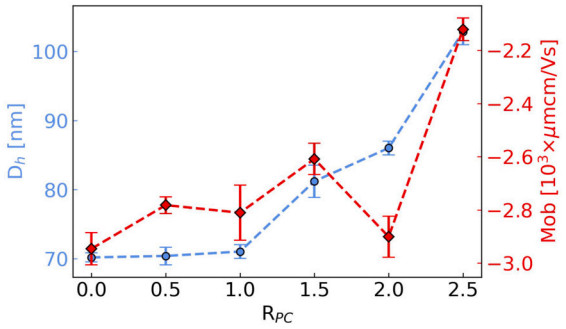

Fig. 2. Hydrodynamic diameter (circles) and electrophoretic mobility (EM, diamonds) measurements of diluted CNC suspensions (0.1% wt.) with increasing amount of PEGDA (0.05-0.25% wt.). The measurements were averaged over 15 cycles for DLS (10 for EM), and over three repetitions. The ionic strength was controlled with a 1 mM NaCl dilution buffer.

shown in the Supporting Information (Figure S2). Despite reaching relatively low PEGDA/CNC ratios (R_{PC} = 0.002), the start of the sigmoidal curve could not be determined. Hence, a more qualitative data analysis is presented, in place of a data fit with the Langmuir isothermal model.

First, a theoretical calculation was carried out to estimate the R_{PC} value required to saturate the surface of one CNC by PEGDA molecules, following the example reported by Navon and colleagues [27]. The details can be found in the Supporting Information. By assuming that the polymer adsorbed as a sphere, the calculations returned R_{PC} = 0.10, in close agreement with the plateau R_{PC} value observed in Fig. 1.

The adsorption of neutral polymers on nanocelluloses in solution is often attributed to the entropic gain of releasing solvent molecules from both the polymer and the nanocellulose surface, both in aqueous and apolar media [28–30]. Since specific data on the interactions between PEGDA molecules on cellulose surfaces is currently missing, some parallels can be drawn from the studies on PEG and CNCs. The adsorption of PEG in solution is still being debated, with the work of Reid et al. (2017) demonstrating that PEG of various molecular weights (0.3-10 kDa) did not interact through hydrogen bonding with CNCs in the ITC experiment [31]. While other research groups reported the adsorption of PEG molecules, the authors justified these discrepancies by considering the nanoscale effects, and the occurrence of hydrophobic edges on CNCs [31,16]. In this regard, Holappa and colleagues reported that the chemical modification of PEG chains with hydrophobic end-groups allowed their adsorption on cellulose substrates [32]. The presence of diacrylate moieties in PEGDA might contribute similarly to their adsorption on CNCs.

The current investigation on the PEGDA-CNC suspensions corroborates the absence of hydrogen bonding-driven interactions, supporting instead the role of solvent entropy in the adsorption of this PEG derivative on CNCs.

The interaction was also investigated with QCM-D measurements (Supporting Information Figure S3). Following the formation of a CNC layer, the injection of the polymer solution had a modest, yet visible shift in the dissipation and resonance frequency. The following rinsing by the buffer solution resulted in a comparable shift in the opposite direction for both Δf and ΔD, suggesting that the layer of adsorbed PEGDA was partially removed. This could be attributed to the relatively weak physiadsorption exhibited by the polymer on the CNCs. Nevertheless, after rinsing the QCM-D cell with the buffer solution, another CNC injection was performed, showing a decrease in resonance frequency and an increase in the dissipation. This observation was attributed to the formation of a second CNC layer on the newly PEGDA surface, previously injected and adsorbed. While the evidence was indirect, the results from this experiment also supported the interaction between the polymer and CNCs.

Further insights were provided by dynamic light scattering (DLS) and electrophoretic mobility (EM) measurements, presented in Fig. 2. The average hydrodynamic diameter (D_h) and EM of a pure CNC suspension were 70.2 nm and -2946 μm·cm/Vs (corresponding to a ζ-potential of -42.5 mV, using the Smoluchowski equation and assuming the particles to be spheres), respectively, in line with literature reports for commercial CNCs produced by acid hydrolysis [22]. Up to R_{PC} = 1, the addition of PEGDA did not affect significantly the D_h, whereas a modest increase in EM was detected. Further amounts of polymer caused instead a steep increase in the D_h (102.9 nm) and an increase in EM to -2121 μm·cm/Vs (ζ-potential = -30.0 mV). The corresponding variations in EM with PEGDA were likely affected by the increase in D_h, rather than a significant electrical double-layer screening by a low-molecular weight, neutral polymer such as PEGDA (0.7 kDa) [33]. Considering the radius of gyration of PEGDA (*ca.* 1 nm), it's likely that its adsorption on the surface of CNCs, up to R_{PC} = 1, did not impact on their D_h. Larger amounts of PEGDA (R_{PC} > 1), on the other hand, resulted in a larger surface coverage of the CNCs, increasing their apparent diameter. By considering the behaviour observed in the QCM-D experiments (Supporting Information Figure S3), it is also possible that PEGDA caused bridging and aggregation of CNCs, which would also explain the larger D_h. Polymer-induced depletion might also be occurring. Nevertheless, all samples maintained sufficiently high ζ-potential values to ensure the colloidal stability of nanoparticles; while it was not evaluated at this point, the presence of a polymer layer could also contribute to a steric stabilization of the CNCs.

To confirm the nature of this interaction, additional analyses were carried out on concentrated suspensions (8% wt. CNC) with FT-IR (Supporting Information Figure S4). The higher concentration in these samples was necessary to ensure a sufficient signal-to-noise ratio. The position of the carbonyl and acrylate stretching bands of PEGDA was not affected when mixed with CNCs, excluding the occurrence of hydrogen bonding with the cellulose surface. Similar results were also reported by Andrew and coworkers for CNC suspensions with PEG or polyvinylpyrrolidone (PVP), a neutral polymer containing a carbonyl moiety in its backbone [34].

In summary, PEGDA was found to interact and adsorb on the surface of CNCs, as demonstrated by combined ITC, QCM-D and DLS experiments. The driving force for the adsorption was attributed to the release of bound solvent molecules from the cellulose surface and the polymer, in line with previous reports for neutral polymers [35,17].

3.2. *Liquid crystalline behaviour of CNCs with PEGDA*

The impact of PEGDA on the self-assembly of CNCs was then investigated. The nanoscale properties of the suspensions were characterized by SAXS (Fig. 3). The 2D SAXS patterns were isotropic, indicating no preferential orientation of the CNC domains with respect to the incident X-Ray beam (Supporting Information Figure S5). All samples displayed a first-order peak around $q^* = 0.2\ nm^{-1}$, corresponding to the repeat-

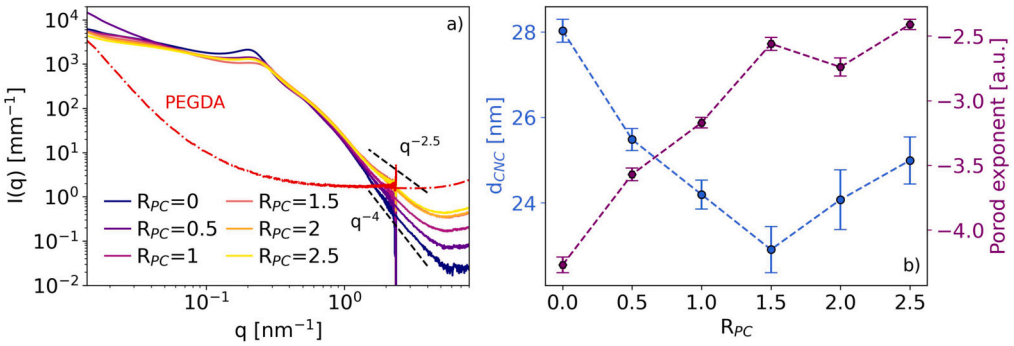

Fig. 3. a) Azimuthally-averaged 1D scattering intensities, obtained by small-angle X-Ray scattering (SAXS) on CNC suspensions (8% wt., 10 mM NaCl) with increasing amounts of PEGDA (0-20% wt.) after 14 days of rest. Pure PEGDA is also included for reference. b) Interparticle distance between CNCs, calculated from the Kratky plot of the 1D scattering intensities (circles), Porod exponent as a function of added PEGDA (diamonds). The values of d_{CNC} and Porod exponent were averaged over 4 points in the capillary.

ing distance between CNCs [36]. Analysis of the related Kratky plots (Supporting Information Figure S6) revealed the presence of a second-order peak for samples R_{PC} = 0-1.5, which suggests that CNCs exhibited a higher-order particle organisation.

The addition of PEGDA had two main effects on the SAXS patterns. First, a shift in the position of q*, resulting in a decrease of the d_{CNC} from 28.0 nm for the pure 8% wt. CNC suspension to 22.8 nm at R_{PC} = 1.5 (Fig. 3b). Further amounts of PEGDA caused a modest increase in d_{CNC}, stabilizing at 24.9 nm for R_{PC} = 2.5. Second, the slope of the Porod region (around q = 1 nm^{-1}) decreased in magnitude from -4 to -2.5 as R_{PC} increased from 0 to 1.5, remaining approximately constant at this value up to R_{PC} = 2.5. This change in the Porod exponent could potentially result from the linear combination of the scattering of PEGDA (red dotted line in Fig. 3a) and the CNCs. However, if this were the case, the observed trend in Fig. 3b would be expected to increase monotonically with the amount of added polymer. Instead, the trend plateaued at R_{PC} = 1.5. This suggests that the variation in the Porod exponent is associated with a transition from smooth to rough interface scattering, which may indicate adsorption of PEGDA onto CNCs. An important point is that, as the scattered intensity I(q) is the multiplication of the form and structure factors (P(q) and S(q), respectively), the trend observed for d_{CNC} in Fig. 3b should be considered qualitatively, as it cannot be determined with absolute precision.

The colloidal stability of CNCs, which is reflected in their interparticle distance, is mainly attributed to the electrostatic stabilization of CNCs endowed by charged groups on their surface. However, adsorbed or grafted polymers can also play a role through steric stabilization [37,33,38,39]. As the concentration of CNCs and ionic strength were fixed (10 mM NaCl), the trend observed for d_{CNC} was likely driven by the presence of PEGDA molecules.

The behaviour observed for PEGDA used in this work is in contrast with other cases of neutral polymer additives with CNCs. In the work of Sun and colleagues, the presence of PEG (20 and 200 kDa) at a R_{PC} close to 1 (3.5% CNC and 4% PEG wt.) caused a broadening of the interparticle distance peak, and the disappearance of second-order reflections, without however shifting its position [40]. PEG polymers of larger molecular weight (900 kDa, 1.7% wt.), on the other hand, were seen to reduce the d_{CNC} (from 48.7 to 44.0 nm) of a 4% wt. CNC suspension [41]. These variations were attributed to an increasing depletion phenomenon, which positively correlated with the molecular weight of the added PEG. In the case of xyloglucan (20 kDa) added to CNCs, Voisin and co-workers reported no significant variation of d_{CNC} for R_{PC} between 0 and 0.5; nevertheless, at the highest XG concentration (R_{PC} = 0.5) a slight reduction of d_{CNC} could be seen, as well as the loss of the second-order reflection [39].

Based on current results and previous works, PEGDA molecules are likely adsorbing on the surface of CNCs, and inducing simultaneously a reduction of d_{CNC} already at R_{PC} = 0.5, owing to their smaller molecular weight and gyration radius (ca. 1 nm), compared to larger polymers. The decrease in d_{CNC} may be related to the blurring of the chiral features of the CNCs by the polymer; larger amounts of PEGDA, on the other hand, effectively induced some degree of steric stabilization, considering the increase in d_{CNC} for R_{PC} = 2-2.5. While the amount of PEGDA in the suspensions reached a significant mass fraction (up to 20% and a R_{PC} = 2.5), it is not clear whether a depletion interaction is also occurring in the system. In fact, previous works showed that PEG molecules of 1 kDa did not trigger such a phenomenon in the case of a lipid bilayer system [42].

The self-assembly of CNCs in presence of PEGDA was then investigated at the microscale using PLM (Fig. 4).

All samples contained brightly coloured and dark regions. The detection of cholesteric phases by PLM depends on the orientation of the helicoidal axis relative to the observation direction. When the helicoidal axis is nearly parallel to the observation direction, the birefringence is averaged over the continuous turn of the helix, resulting in poor contrast. Conversely, when the helicoidal axis is perpendicular to the observation direction, the birefringence is extinguished, yielding high contrast and allowing the visualization of the fingerprint pattern [43]. Samples R_{PC} = 0-1.5 featured filamentous structures, similar to the ones published by Azzam and coworkers for CNCs grafted with polyetheramine [44]. Samples with larger amounts of PEGDA (R_{PC} = 2-2.5) instead appeared as a continuous birefringent region. Higher magnification of the birefringent domains (insets of Fig. 4) revealed the characteristic fingerprint pattern of the cholesteric phases. Hence, in the range of concentrations explored in this work, the presence of PEGDA did not trigger depletion phenomena, nor hamper the formation of CNC cholesteric structures.

Additional insights into the behaviour of CNC/PEGDA suspensions were inferred by measuring the anisotropic volume fraction (ϕ_{ani}), and by SALS experiments on the quartz capillaries (Fig. 5). The initial CNC suspension (8% wt., R_{PC} = 0) was found in a biphasic state with $\phi_{ani} \approx$ 0.8, consistent with literature reports [22]. The addition of PEGDA to the CNC suspension first caused a decrease in ϕ_{ani} for R_{PC} = 0.5-1, returning to 0.8 at R_{PC} = 1.5. Larger amounts of polymer increased ϕ_{ani}, reaching a full anisotropic state at R_{PC} = 2.5. The phase behaviour of CNC/PEGDA mixtures contrasts the one reported for non-adsorbing polymers, such as high-molecular weight dextran (2000 kDa) and PEG (200 kDa). In both cases, progressive additions of polymer did not affect ϕ_{ani} in biphasic CNC suspension at fixed particle concentration. The presence of dextran, however, changed the repartition of CNCs between the isotropic and anisotropic phase (from 9.94% wt. to 9.03% wt. in the isotropic phase at 1.2 µmol L^{-1} dextran concentration), due to the exclusion between nanorods and polymer coils (R_g = 34 nm) [45]. In the case of PEG 200 kDa, a nematic phase was observed instead of a cholesteric structure, owing to depletion forces overcoming electrostatic stabilization and thus restricting the movement of CNCs [40].

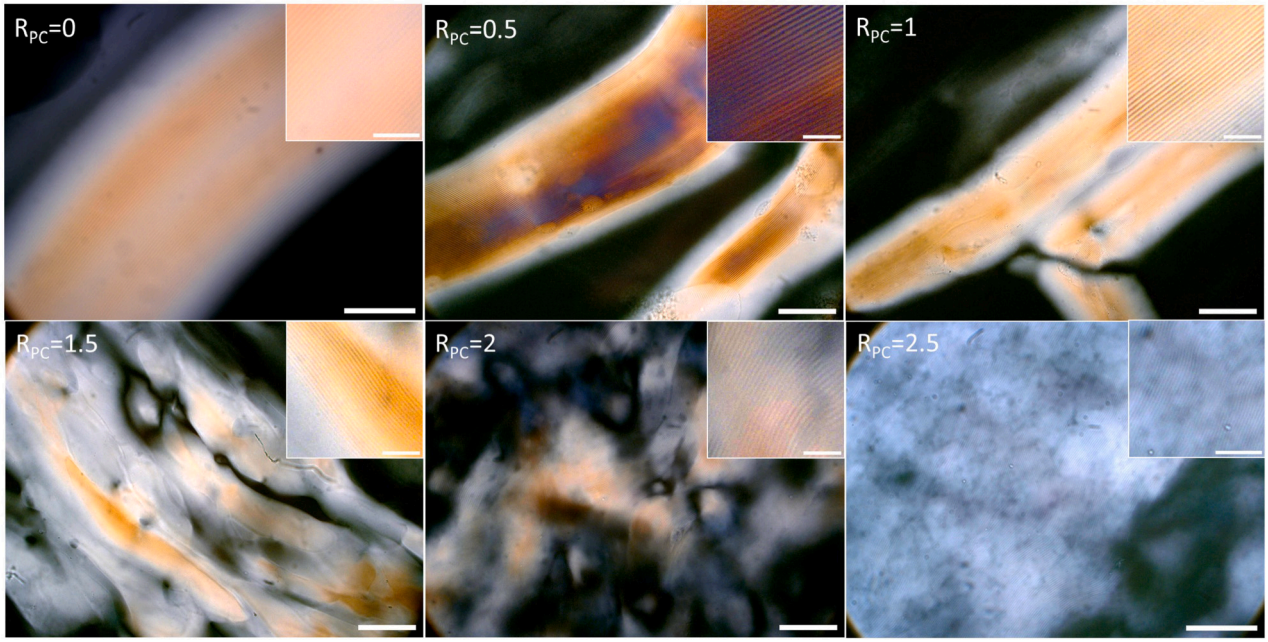

Fig. 4. Polarized light microscopy (PLM) images of aqueous CNC suspensions (8% wt., 10 mM NaCl) with increasing amounts of PEGDA (0-20% wt.), sealed in microscope slides for 7 days. The scale bar of the main images is 100 μm, whereas in the insets is 10 μm.

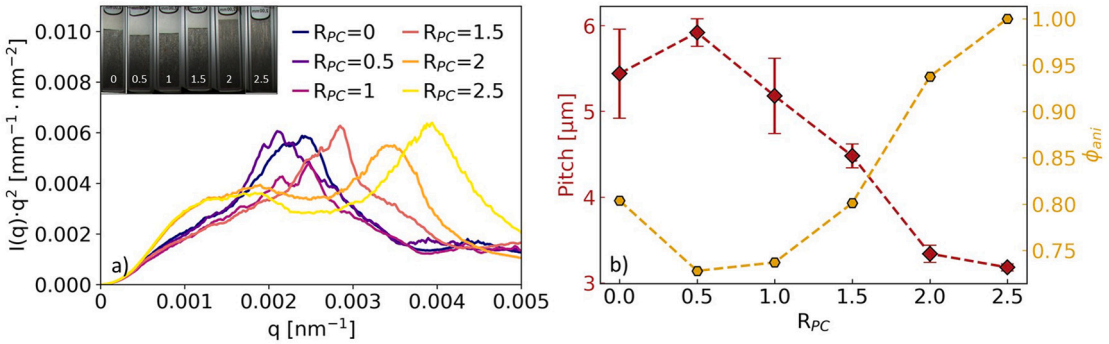

Fig. 5. a) Kratky plots obtained from small-angle light scattering (SALS) experiments on quartz cuvettes (inset), showing the presence of a peak (q^{**} corresponding to $P/2$). b) Mean cholesteric pitch (P), averaged over 5 points in the quartz cuvette, and anisotropic volume fraction (ϕ_{ani}) as a function of R_{PC}.

Concerning the SALS measurements, all samples displayed a circular diffraction pattern between q = 0.002 and q = 0.004 nm^{-1}, representing the cholesteric half-pitch repeating distance ($P/2$) (Supporting Information Figure S7). The trend of the cholesteric pitch was specular to the variation in ϕ_{ani}, increasing from 5.4 to 5.9 μm at R_{PC} = 0.5, followed by a continuous decrease to 3.2 μm at R_{PC} = 2.5, in agreement with the values obtained by PLM (Supporting Information Figure S8). In fact, Zhang and co-workers reported a gradual increase in P when adding PEGDA 0.7 kDa to a CNC suspension between R_{PC} = 0 and 0.5 [46], confirming and complementing the trend observed in Fig. 5b.

The behaviour of the PEGDA/CNC suspensions at R_{PC} > 0.5 shared some similarities with suspensions of polymer-grafted CNCs. Araki et al. (2001) reported that PEG-grafted (1 kDa) CNCs displayed shorter pitch distances compared to the carboxylated counterpart (4.0 vs 7.0 μm), attributed to the reduced surface charge following the grafting reaction [37]. Azzam and co-workers studied in detail the behaviour of aqueous suspensions of CNCs grafted with polyetheramines (0.6–2 kDa) [44]. Similarly to Araki et al. (2001), polymer-grafted CNCs displayed shorter pitch values compared to sulfated CNCs between 3.5 and 5.2% vol., and a higher ϕ_{ani} at all CNC volume fractions. Here, the authors concluded that the grafted polymer chains enhanced the transmission of chirality from the CNC core [44]. In a following publication, the conformation of the grafted polyetheramines was deduced from small-angle neutron scattering experiments, revealing that the polymers assumed a Gaussian coil structure on the surface of the CNCs [47]. While information about the conformation of PEGDA on CNCs is not available at this stage, it can be assumed that the progressive adsorption of polymer chains produced nanorods with bulkier morphologies than bare CNCs, resulting in higher particle volume fractions.

The observed trends at the nano, micro and macro scale (d_{CNC}, P and ϕ_{ani}, respectively) of the CNC/PEGDA suspensions can be related and expressed with the twist angle between the CNCs, θ_{CNC} [36] (Eq. (3)):

$$\theta_{CNC} = (360 \cdot d_{CNC})/P \tag{3}$$

Furthermore, the cholesteric pitch can also be expressed in its reciprocal form as the cholesteric wavevector (here γ to avoid ambiguity with q), which is related to the helical twisting power (HTP) and the concentration of chiral dopant c [48,49] (Eq. (4))

$$\gamma = 2\pi/P = HTP \cdot c \tag{4}$$

For CNCs, the presence of twisted nanocrystal bundles has been proposed in the role of the dopant [49]. As in samples R_{PC} = 0-2.5 the amount of CNCs was fixed, c can be considered constant. Combining

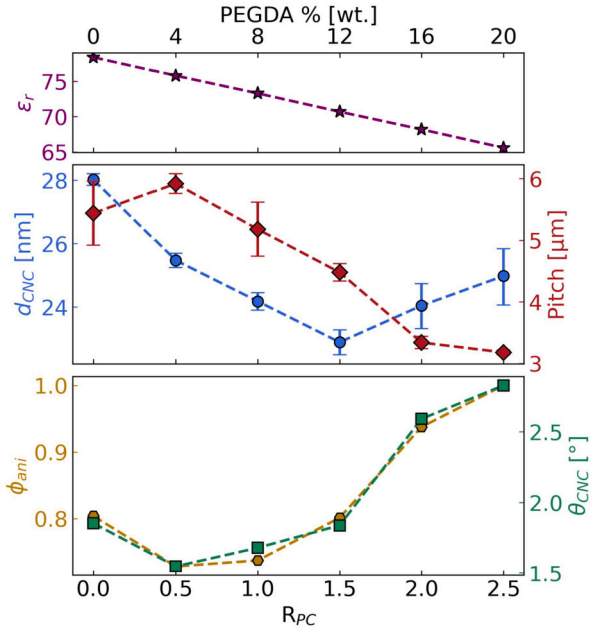

Fig. 6. Estimated relative dielectric permittivity as a function of added PEGDA (ϵ_r, stars), calculated from the reference value for PEG 0.6 kDa from [50]. Interparticle distance between CNCs (d_{CNC}, circles) and cholesteric pitch (*P*, diamonds) of CNCs suspensions (8% wt.) with increasing amounts of PEGDA (0-20% wt.), obtained from SAXS and SALS measurements, respectively. Anisotropic volume fraction (ϕ_{ani}, hexagons) and twist angle between CNCs (θ_{CNC}, squares), measured from polarized images of the quartz cuvettes and calculated according to Eq. (3), respectively.

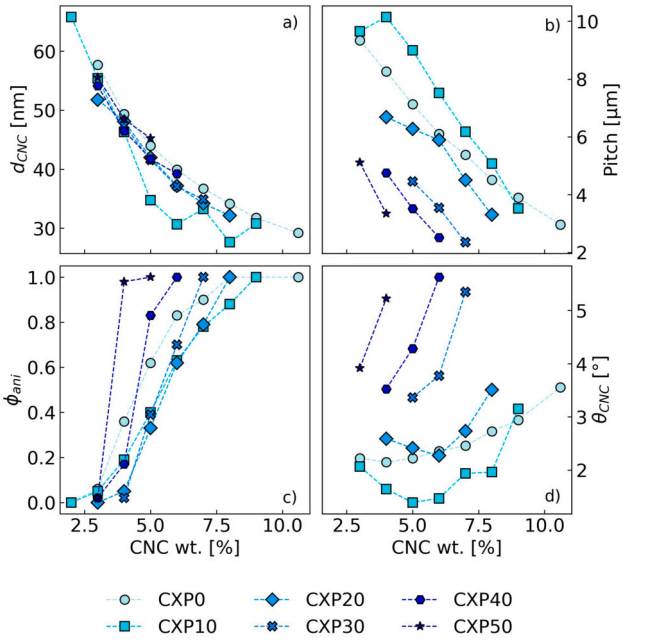

Fig. 7. Results from the multi-scale investigation of CNC and PEGDA suspensions, as a function of CNC and PEGDA concentrations. a) Interparticle distance (d_{CNC}) calculated from the first-order peak of the azimuthally-averaged SAXS patterns b) cholesteric pitch (*P*) measured from azimuthally-averaged SALS patterns c) anisotropic volume fraction (ϕ_{ani}), measured using polarized photography of the samples in quartz cuvettes and d) CNC twist angle (θ_{CNC}) calculated from the d_{CNC} and *P* values. The samples are grouped according to the quantity of PEGDA present in the suspension: 0% (CXP0, circles), 10% (CXP10, squares), 20% (CXP20, rhombi), 30% (CXP30, crosses), 40% (CXP40, hexagons) and 50% (CXP50, stars).

Eq. (3) and Eq. (4) shows that the twist angle is proportional to the interparticle distance and the *HTP* (Eq. (5))

$$\theta_{CNC} \propto d_{CNC} \cdot HTP \tag{5}$$

The relation between *HTP* and θ_{CNC} against ϕ_{ani} was also explored (Supporting Information Figure S9). Both parameters displayed a linear correlation with ϕ_{ani}; however, θ_{CNC} correlated slightly better than *HTP*, suggesting that incorporating d_{CNC} (the interparticle distance) improved the description of the phenomena occurring in the CNC/PEGDA mixtures. Therefore, the trend observed for the distance between particles by SAXS (Fig. 3b), though initially considered qualitative due to the multiplication between P(q) and S(q), was corroborated by systematic variations in θ_{CNC} and ϕ_{ani} at higher concentrations of PEGDA. A plot of ϕ_{ani} and θ_{CNC} as a function of R_{PC} is presented in Fig. 6.

The variations in θ_{CNC} can be used to interpret the changes in the CNC suspension as more PEGDA was added to the mixture. As a reminder, the twist angle between neighbouring CNCs is the result of multiple contributions, both enthalpic and entropic in origin. The electrostatic potential is minimized at perpendicular orientations, while van der Waals forces promote the parallel arrangement of CNCs [51–53]. In turn, the system lowers its energy when the rods are packed in a way that maximizes their mobility and the resulting free volume [54,36]. Furthermore, the shape of the particles also affects their packing [55].

At $R_{PC} = 0.5$, the decrease in θ_{CNC} could be attributed to the adsorption of PEGDA on the surface of CNCs, which blurred the chirality of the nanoparticles and therefore resulted in a lower *HTP* (larger *P*). In fact, as PEGDA did not cause significant changes in the EM (Fig. 2), this variation likely lied in the morphology of the CNCs, and in the associated change in the packing entropy. Between $R_{PC} = 1$ and 1.5, the layer of adsorbed PEGDA molecules became denser, turning the initial weakening into a stronger chiral transmission, ascribed to a simultaneous change in particle morphology and higher volume fraction, with θ_{CNC} increasing back to 1.9°. At $R_{PC} > 1.5$, the saturation of CNCs' surface by PEGDA chains was likely reached (*cfr.* Porod exponent in Fig. 3b); however, θ_{CNC} kept increasing due to the variation in the dielectric constant of the medium becoming predominant with added polymer. In fact, ϵ_r decreased from 78.4 to 65.6 for 20% wt. PEGDA (Fig. 6, stars). This variation was also reflected in d_{CNC}, increasing again due to the stronger electrostatic interaction related to the change in the properties of the medium. Notably, the sharp change in θ_{CNC} (from 1.9 to 3.3°) at $R_{PC} > 1.5$, supports this hypothesis, suggesting that the added PEGDA may be present in the suspension medium between CNCs, rather than being adsorbed on the surface of the nanoparticles.

The multi-scale approach used above was extended to a larger range of CNC and PEGDA concentrations, aiming to verify the trends observed for the suspensions at 8% wt. CNC concentration. The results are shown in Fig. 7.

The values of d_{CNC} for a fixed PEGDA quantity decreased following a power law of $C^{-0.54}$, close to the -1/2 exponent previously reported in the literature [56]. Notably, CXP10 samples displayed a shorter interparticle distance between 5 and 7% wt. compared to the native suspension (CXP0) and to CXP20-CXP50 samples. The trend observed in Fig. 3b was confirmed; interestingly, the changes in d_{CNC} became less pronounced above 20% wt. PEGDA for the same CNC concentration. The variations in *P* (Fig. 7b) exhibited the same behaviour as the one in Fig. 5b: an expansion of the cholesteric pitch for CXP10 samples, followed by a compression with PEGDA amounts above 20% wt. (CXP20-CXP50). The anisotropic phase volume fraction (Fig. 7c) showed the typical sigmoidal behaviour reported for CNC suspensions [4] as a function of concentration. When PEGDA was added (CXP10), the curve shifted to higher CNC concentration, indicating a delay in the onset of the fully anisotropic phase. In contrast, samples with higher PEGDA content (CXP20-CXP50) exhibited a progressively narrower biphasic region, with the transition to a fully anisotropic phase occurring at lower CNC concentrations (see also Supporting Information Figure S10).

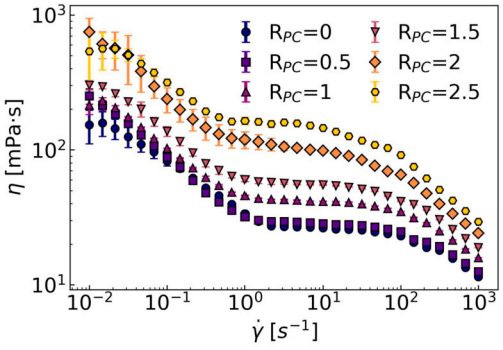

Fig. 8. Flow curves of CNC suspensions (8% wt.) with increasing amounts of PEGDA (0-20% wt.) and fixed ionic strength (10 mM NaCl), after 7 days of rest. The viscosity was measured starting from 0.01 s^{-1} to 1000 s^{-1}. The error bars represent the standard deviation of three measurements.

Finally, the values of θ_{CNC} (Fig. 7d) generally increased with CNC concentration within the same CXPY series, as already reported by Schütz and colleagues [36]. In line with previous observations, the CXP10 samples displayed lower θ_{CNC} values between 3 and 8% wt. compared to the other samples. In general, these results are consistent with the trend observed in Fig. 6 for the 8% wt. CNC samples, highlighting the presence of two main regimes based on the amount of PEGDA.

This behaviour resembles the one described by Attia et al. (2020), where the authors explored the phase diagram of CNCs in concentrated ethylene glycol (EG) / water mixtures [57]. The difference in the magnitude of variation for θ_{CNC} and *P* for samples CXP20-CXP50 was attributed to the permanence of a nanometre-sized water layer around the CNCs [58]. As such, the effect arising from the decrease in dielectric constant levelled off for interparticle interactions at higher amounts of polymer, while the cholesteric structures were more affected by the bulk properties of the solvent, owing to their larger (micrometre) dimensions. Similarly, the critical concentration for the biphasic and anisotropic transitions (C_i and C_a) were predicted to occur at lower CNC amounts with lower dielectric permittivities [53]. The calculated ϵ_r values for the CXP0-CXP50 samples are available in the Supporting Information (Table S1).

Despite the presence of other factors, such as the possibility of depletion interactions occurring at large amounts of PEGDA (30-50% wt., above the polymer overlap concentration [42]), and the variation in the ionic strength (0.22-1 mM NaCl, see Supporting Information Table S2) for this set of samples, the results presented in Fig. 7 aligned with this hypothesis.

3.3. Rheo-optical characterization of CNC/PEGDA suspensions

To complete the characterization of the system, the flow properties of the CNC/PEGDA suspensions were determined using rheometry (Fig. 8). All samples displayed the characteristic three-region viscosity profile, typically observed for aqueous suspensions of CNCs [59]. In the first region (0.01 and 1 s^{-1}), the viscosity decreased with increasing shear rate, corresponding to the orientation of cholesteric domains along the flow direction. This shear-thinning behaviour was followed by a nearly Newtonian plateau (1-100 s^{-1}) where the size of the cholesteric domains was progressively reduced. The third shear-thinning region (100 to 1000 s^{-1}) represents the disruption of the cholesteric structure in favour of a nematic alignment [24,23]. The rheological measurements thus confirmed the presence of cholesteric structures for all PEGDA amounts. Interestingly, the viscosity difference between R_{PC} = 0-0.5 samples was almost negligible. However, larger amounts of PEGDA significantly increased the viscosity between samples R_{PC} = 1 to 2.5 by almost one order of magnitude. This could result from an interplay between the weakening of the chiral interactions in the cholesteric structure, and the intrinsic higher viscosity of pure PEGDA (*ca.* 100 mPa·s) at R_{PC} = 0.5.

In the third shear-thinning region (100-1000 s^{-1}), viscosity differences between the samples became smaller. This could result from the disruption of cholesteric domains into nematic phases [24], where the difference in *HTP* between samples was negligible.

The rheological analysis focused then on the dynamics of cholesteric structure recovery, using a rheo-optical setup. This enabled the simultaneous observation of the rheological parameters and microstructure after applying high shear. The results are shown in Fig. 9 and Fig. 10.

Recovery experiments revealed that samples with R_{PC} = 0-2 exhibited a liquid-like behaviour (G" > G'), whereas sample R_{PC} = 2.5 exhibited a gel-like behaviour (G'>G"). After applying shear at 1000 s^{-1}, the G' and G" increased exponentially, however in two distinct phases: the first one lasting between 0 and approximately 200 s, and the second phase extending from 200 s to the end of the measurement at 3600 seconds (Fig. 9c and d). Sample R_{PC} = 2.5 showed instead a continuous increase in G' throughout the experiment, while G" stabilized around 200 s and oscillated around *ca.* 15 Pa. Microscopy observations at 1000 s^{-1} (Fig. 10, first row) displayed a bright, striped colouration, due to the transient alignment of the CNCs under the shear imposed by the rheometer plates. The CNCs act then as a birefringent plate upon interference with visible light [59].

The appearance of sample R_{PC} = 0 evolved by changing the intensity of the transmitted colours (see Movie 1 of the Supporting Information), eventually displaying the fingerprint pattern around 150 seconds (Fig. 10). This signalled the isotropic-to-cholesteric transition for the CNCs; the fingerprint pattern persisted and compacted over time. Samples R_{PC} = 0.5-2 exhibited a similar behaviour, except for a delay in the development of the fingerprint structure compared to R_{PC} = 0 (see Movie 2 to Movie 5 in the Supporting Information). In contrast, sample R_{PC} = 2.5 did not display a significant change in the microstructure throughout the experiment, with the fingerprint not appearing in these microscopy observations (Movie 6 from the Supporting Information). This observation was consistent with the gel-like nature of the sample and, compared with the results of SALS and PLM, suggests that the higher viscosity delayed the kinetics of cholesteric formation from the isotropic state.

For samples R_{PC} = 0-2, the pitch could be measured as a function of time during the rheological measurements. The complex modulus G* and the pitch of these samples are plotted in Fig. 11. The complex modulus was plotted to capture the variations of both G' and G", and was compared with the measured pitch for the different samples. Consistent with previous data, G* exhibited two distinct recovery regimes. The fingerprint pattern of the cholesteric liquid crystals became detectable at the onset of the second phase, in agreement with the behaviour reported for anisotropic CNC suspensions [24]. The pitch values consistently decreased with time across all samples, showing that the reformation of the cholesteric liquid crystals involved the compression of the helicoidal planes until a constant value was achieved at the end of the experiment. Some interesting trends could be discovered.

Firstly, the appearance of the fingerprint structure and stabilization of the pitch size were progressively delayed with increasing amounts of PEGDA. For R_{PC} = 0, the pitch was first detected around 150 s with an approximate value of 12 µm, stabilizing at 8 µm after 300 s. For samples R_{PC} = 0.5-1, the pitch was also detected around 150 s, stabilizing however at 400 and 500 s, respectively. Samples R_{PC} = 1.5-2 exhibited a detectable fingerprint pattern between 200 and 300 s, reaching a stable pitch between 800 and 1000 s.

Secondly, the final pitch value largely followed the trend observed earlier with PLM and SALS, correlating with the amount of added PEGDA, although the values observed in Fig. 11 were larger. This discrepancy suggests that further time was required for the helicoidal structure to fully tighten to equilibrium. Indeed, SALS measurements carried out on samples after 1 and 7 days confirmed this trend (Supporting Information Figure S8).

The delay on the onset of fingerprint structure, and the shorter pitch values pointed towards a stronger chiral interaction, at the expense of

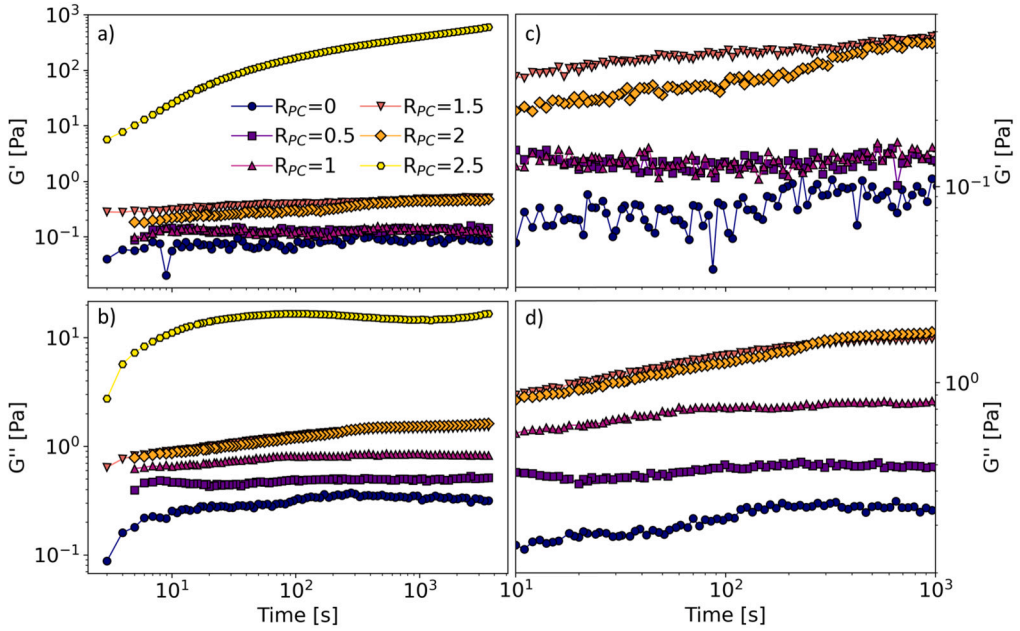

Fig. 9. a) and b) oscillatory rheometry measurements (G' and G", respectively) carried out on 8% wt. CNC suspensions with increasing amounts of PEGDA (0-20% wt.). c) and d) are magnifications of the region between 10 and 1000 s, where the restructuring of CNCs into nematic and cholesteric phases occurred. The measurements were carried out at 1 Hz oscillation frequency and 1% deformation for 1 hour, after 5 minutes of high shear (1000 s^{-1}).

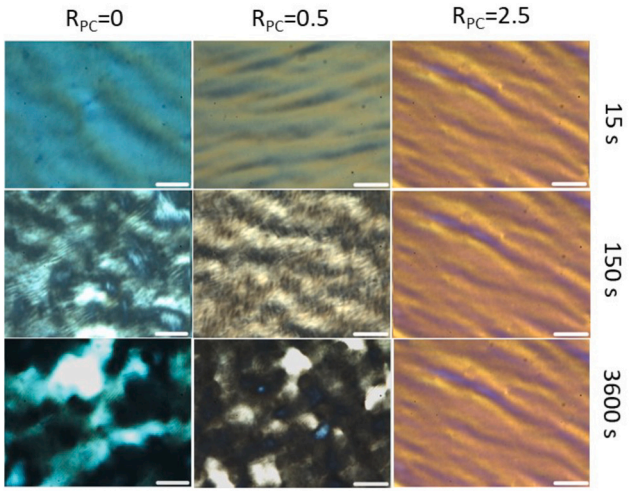

Fig. 10. Polarized light microscopy (PLM) images taken during the oscillatory rheometry experiment of Fig. 9. Scale bar is 50 μm for all samples. The first row shows the appearance of samples 15 s after the shear step of 1000 s^{-1}, the second one after 150 seconds, and the third one at the end of the experiment (3600 seconds) for different CNC/PEGDA ratios (R_{PC} = 0, 0.5 and 2.5).

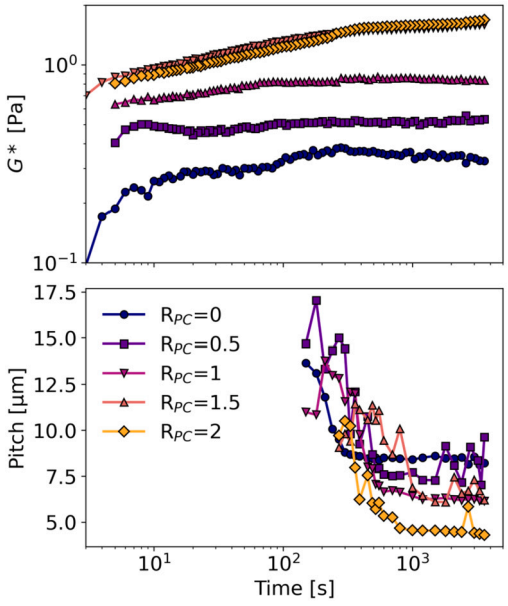

Fig. 11. a) Complex viscosity measured during the oscillation recovery experiment for CNC suspensions with increasing PEGDA (0-20% wt.). b) Mean pitch size for the same samples, calculated through image analysis of 12 PLM images each acquired with the rheo-optical setup.

slower transition kinetics to the cholesteric phase. This effect was particularly pronounced for sample R_{PC} = 2.5, where the pitch could be detected by SALS at least after 24 h.

4. Conclusions

An extensive physicochemical characterization of CNCs and PEGDA suspensions was carried out, using a multi-scale approach. The study revealed that PEGDA molecules adsorbed on the surface of CNCs through non-covalent physiadsorption, preserving the colloidal stability of the nanoparticles over a wide range of concentrations and CNC-PEGDA mass ratios.

For a biphasic CNC suspension at 8% wt., the progressive addition of PEGDA caused first a weakening of the colloidal interactions between the nanoparticles, resulting in a looser cholesteric pitch (P) and a reduction in the anisotropic volume fraction (ϕ_{ani}) at R_{PC} = 0.5. This behaviour was attributed to a blurring of the chiral features of the CNCs caused by the adsorption of PEGDA molecules. Above R_{PC} = 0.5, further polymer adsorption resulted in an enhancement of the helical twisting power, likely resulting from a combined variation in the particle morphology and higher effective CNC volume fraction, similar to the one reported for polymer-grafted CNCs [44]: as a consequence, the cholesteric pitch was reduced, and the anisotropic volume fraction increased. This phenomenon was accompanied by the decrease in dielectric constant of the medium due to the added PEGDA, which contributed to stronger electrostatic interactions between CNCs at R_{PC} = 2-2.5.

The variations in the properties of the suspension, from the nano to the microscale, were effectively captured by the twist angle θ_{CNC}, which was calculated from d_{CNC} and P, exhibiting a strong correlation with ϕ_{ani}.

The investigation was complemented by rheo-optical measurements, which provided further insights into the microstructure of the CNC/PEGDA suspensions. Larger PEGDA concentrations progressively delayed the formation of the cholesteric structure. In particular, in $R_{PC} = 2.5$ samples the formation of the fingerprint was observed after 24 h, in contrast to few minutes for samples with lower amounts of polymer. Due to the widespread use of PEGDA as an additive in the fabrication of CNC-based composites, the information contained in this work are valuable to understand the structure-property relationship of the precursor suspensions, the processing and the properties of the final products.

CRediT authorship contribution statement

Lorenzo Metilli: Writing – review & editing, Writing – original draft, Methodology, Investigation, Formal analysis, Data curation, Conceptualization. **Samuel Mandin:** Writing – review & editing, Validation, Methodology, Formal analysis, Conceptualization. **Ioanna Chazapi:** Writing – review & editing, Validation, Methodology, Formal analysis. **Erwan Paineau:** Writing – review & editing, Validation, Formal analysis. **William Chèvremont:** Writing – review & editing, Validation, Methodology, Formal analysis. **Nicolas Hengl:** Writing – review & editing, Validation, Formal analysis. **Frédéric Pignon:** Writing – review & editing, Visualization, Supervision, Project administration, Methodology, Funding acquisition, Formal analysis. **Bruno Jean:** Writing – review & editing, Validation, Supervision, Project administration, Funding acquisition.

Declaration of competing interest

The authors declare that they have no known competing financial interests or personal relationships that could have appeared to influence the work reported in this paper.

Acknowledgements

The authors would like to thank Vincent Verdoot (LRP) for preparing the rheo-optical setup, and Didier Blésès (LRP) for his insights for measuring the fingerprint pattern from the PLM images.

The authors acknowledge the NanoBio-ICMG Platform (UAR 2607, Grenoble) for granting access to the QCM-D instrument, and acknowledge Liliane Guerente (NanoBio-ICMG) for her help and support in designing the QCM-D experiment. The authors would like also to thank Laurent J. Michot and Delphine Talbot for granting access to the ITC apparatus at the Phenix Laboratory (UMR 8234, Sorbonne University).

ESRF is acknowledged for the provision of synchrotron beamtime (proposal SC-5524 and IH-SC-1832). SOLEIL is acknowledged for the provision of synchrotron beamtime (BAG 20231786 and 20221057).

The authors acknowledge the support of the French Agence Nationale de la Recherche (ANR), under grant agreement #ANR-20-CE43-0015 (ANISOFILM) for financial support of S. Mandin's PhD thesis and L. Metilli's postdoctoral position. LRP is part of LabEx Tec21 (Investissements d'Avenir - grant agreement #ANR-11-LABX-0030). LRP and CERMAV are part of Institut Carnot PolyNat (Investissements d'Avenir - grant agreement #ANR-16-CARN-0025-01), and the Glyco@Alps programme (Investissements d'Avenir - grant agreement #ANR-15-IDEX-02).

Appendix A. Supplementary material

Supplementary material related to this article can be found online at https://doi.org/10.1016/j.jcis.2025.01.155.

Data availability

Data will be made available upon request. Data from ESRF can be found online at https://doi.org/10.15151/ESRF-ES-1553323761.

References

[1] Abdul Hakeem Anwer, Afreen Ahtesham, Mohd Shoeb, Fouzia Mashkoor, Mohd Zahid Ansari, Shushuai Zhu, Changyoon Jeong, State-of-the-art advances in nanocomposite and bio-nanocomposite polymeric materials: a comprehensive review, Adv. Colloid Interface Sci. 318 (August 2023) 102955.

[2] Robert J. Moon, Ashlie Martini, John Nairn, John Simonsen, Jeff Youngblood, Cellulose nanomaterials review: structure, properties and nanocomposites, Chem. Soc. Rev. 40 (7) (2011) 3941.

[3] Kevin De France, Zhihui Zeng, Tingting Wu, Gustav Nyström, Functional materials from nanocellulose: utilizing structure–property relationships in bottom-up fabrication, Adv. Mater. 33 (28) (July 2021) 2000657.

[4] Youssef Habibi, Lucian A. Lucia, Orlando J. Rojas, Cellulose nanocrystals: chemistry, self-assembly, and applications, Chem. Rev. 110 (6) (June 2010) 3479–3500.

[5] Bruno Frka-Petesic, Thomas G. Parton, Camila Honorato-Rios, Aurimas Narkevicius, Kevin Ballu, Qingchen Shen, Zihao Lu, Yu Ogawa, Johannes S. Haataja, Benjamin E. Droguet, Richard M. Parker, Silvia Vignolini, Structural color from cellulose nanocrystals or chitin nanocrystals: self-assembly, optics, and applications, Chem. Rev. 123 (23) (December 2023) 12595–12756.

[6] Kevin J. De France, Chiral nematic cellulose nanocrystal composites: an organized review, Can. J. Chem. Eng. 102 (8) (August 2024) 2695–2713.

[7] Qianqian Wang, Wen Niu, Shixuan Feng, Jun Liu, Huan Liu, Qianqian Zhu, Accelerating cellulose nanocrystal assembly into chiral nanostructures, ACS Nano 17 (15) (August 2023) 14283–14308.

[8] Brody A. Frost, Bradley P. Sutliff, Patrick Thayer, Michael J. Bortner, E. Johan Foster, Gradient poly(ethylene glycol) diacrylate and cellulose nanocrystals tissue engineering composite scaffolds via extrusion bioprinting, Front. Bioeng. Biotechnol. 7 (October 2019) 280.

[9] Kai Hou, Yan Li, Yao Liu, Ruihui Zhang, Benjamin S. Hsiao, Meifang Zhu, Continuous fabrication of cellulose nanocrystal/poly(ethylene glycol) diacrylate hydrogel fiber from nanocomposite dispersion: rheology, preparation and characterization, Polymer 123 (August 2017) 55–64.

[10] Napolabel B. Palaganas, Joey Dacula Mangadlao, Al Christopher C. De Leon, Jerome O. Palaganas, Katrina D. Pangilinan, Yan Jie Lee, Rigoberto C. Advincula, 3D printing of photocurable cellulose nanocrystal composite for fabrication of complex architectures via stereolithography, ACS Appl. Mater. Interfaces 9 (39) (October 2017) 34314–34324.

[11] Jun Yang, Chun-Rui Han, Jiu-Fang Duan, Feng Xu, Run-Cang Sun, Mechanical and viscoelastic properties of cellulose nanocrystals reinforced poly(ethylene glycol) nanocomposite hydrogels, ACS Appl. Mater. Interfaces 5 (8) (April 2013) 3199–3207.

[12] Kai Feng, Guodan Wei, Yubo Liu, Yang Wu, Feng Zhou, Cellulose nanocrystals chiral nematic coating with reversible multiple-stimuli-responsive coloration, ACS Sustain. Chem. Eng. 11 (22) (June 2023) 8374–8385.

[13] Yiyan Huang, Gaowen Chen, Qianmin Liang, Zhuanggang Yang, Huifang Shen, Multifunctional cellulose nanocrystal structural colored film with good flexibility and water-resistance, Int. J. Biol. Macromol. 149 (April 2020) 819–825.

[14] Tianhang Wu, Jiada Li, Juntao Li, Simin Ye, Jie Wei, Jinbao Guo, A bio-inspired cellulose nanocrystal-based nanocomposite photonic film with hyper-reflection and humidity-responsive actuator properties, J. Mater. Chem. C 4 (41) (2016) 9687–9696.

[15] Samuel Mandin, Lorenzo Metilli, Mohamed Karrouch, Christine Lancelon-Pin, Jean-Luc Putaux, William Chèvremont, Erwan Paineau, Nicolas Hengl, Bruno Jean, Frédéric Pignon, Chiral nematic nanocomposites with pitch gradient elaborated by filtration and ultraviolet curing of cellulose nanocrystal suspensions, Carbohydr. Polym. 337 (August 2024) 122162.

[16] Michael S. Reid, Marco Villalobos, Emily D. Cranston, The role of hydrogen bonding in non-ionic polymer adsorption to cellulose nanocrystals and silica colloids, Curr. Opin. Colloid Interface Sci. 29 (May 2017) 76–82.

[17] Malin Wohlert, Tobias Benselfelt, Lars Wågberg, István Furó, Lars A. Berglund, Jakob Wohlert, Cellulose and the role of hydrogen bonds: not in charge of everything, Cellulose 29 (1) (January 2022) 1–23.

[18] Michael S. Reid, Marco Villalobos, Emily D. Cranston, Benchmarking cellulose nanocrystals: from the laboratory to industrial production, Langmuir 33 (7) (February 2017) 1583–1598.

[19] Julian S. Taurozzi, Vincent A. Hackley, Mark R. Wiesner, Ultrasonic dispersion of nanoparticles for environmental, health and safety assessment – issues and recommendations, Nanotoxicology 5 (4) (December 2011) 711–729.

[20] Mélanie Girard, David Vidal, François Bertrand, Jason R. Tavares, Marie-Claude Heuzey, Evidence-based guidelines for the ultrasonic dispersion of cellulose nanocrystals, Ultrason. Sonochem. 71 (March 2021) 105378.

[21] Marcus A. Johns, Cindy Lam, Behzad Zakani, Luke Melo, Edward R. Grant, Emily D. Cranston, Comparison of cellulose nanocrystal dispersion in aqueous suspension via new and established analytical techniques, Cellulose 30 (13) (September 2023) 8259–8274.

[22] Samuel Mandin, Lorenzo Metilli, Mohamed Karrouch, Didier Blésès, Christine Lancelon-Pin, Pierre Sailler, William Chèvremont, Erwan Paineau, Jean-Luc Putaux, Nicolas Hengl, Bruno Jean, Frédéric Pignon, Multiscale study of the chiral self-assembly of cellulose nanocrystals during the frontal ultrafiltration process, Nanoscale 16 (40) (2024) 19100–19115.
[23] Frédéric Pignon, Enrico F. Semeraro, William Chèvremont, Hugues Bodiguel, Nicolas Hengl, Mohamed Karrouch, Michael Sztucki, Orientation of cellulose nanocrystals controlled in perpendicular directions by combined shear flow and ultrasound waves studied by small-angle X-ray scattering, J. Phys. Chem. C 125 (33) (August 2021) 18409–18419.
[24] Frédéric Pignon, Mathilde Challamel, Antoine De Geyer, Mohamad Elchamaa, Enrico F. Semeraro, Nicolas Hengl, Bruno Jean, Jean-Luc Putaux, Erwan Gicquel, Julien Bras, Sylvain Prevost, Michael Sztucki, Theyencheri Narayanan, Henda Djeridi, Breakdown and buildup mechanisms of cellulose nanocrystal suspensions under shear and upon relaxation probed by SAXS and SALS, Carbohydr. Polym. 260 (May 2021) 117751.
[25] Peter Boesecke, Reduction of two-dimensional small- and wide-angle X-ray scattering data, J. Appl. Crystallogr. 40 (s1) (January 2007) s423–s427.
[26] Michael Sztucki, SAXSutilities2: a graphical user interface for processing and analysis of Small-Angle X-ray Scattering data, September 2021, Language: en.
[27] Yotam Navon, Harisoa Radavidson, Jean-Luc Putaux, Bruno Jean, Laurent Heux, PH-sensitive interactions between cellulose nanocrystals and DOPC liposomes, Biomacromolecules 18 (9) (September 2017) 2918–2927.
[28] Salvatore Lombardo, Wim Thielemans, Thermodynamics of adsorption on nanocellulose surfaces, Cellulose 26 (1) (January 2019) 249–279.
[29] Katri, S. Kontturi, Karolina Biegaj, Andreas Mautner, Robert T. Woodward, Benjamin P. Wilson, Leena-Sisko Johansson, Koon-Yang Lee, Jerry Y.Y. Heng, Alexander Bismarck, Eero Kontturi, Noncovalent surface modification of cellulose nanopapers by adsorption of polymers from aprotic solvents, Langmuir 33 (23) (June 2017) 5707–5712.
[30] Saina Kishani, Tobias Benselfelt, Lars Wågberg, Jakob Wohlert, Entropy drives the adsorption of xyloglucan to cellulose surfaces – a molecular dynamics study, J. Colloid Interface Sci. 588 (April 2021) 485–493.
[31] Michael S. Reid, Heera S. Marway, Camila Moran-Hidalgo, Marco Villalobos, Emily D. Cranston, Comparison of polyethylene glycol adsorption to nanocellulose versus fumed silica in water, Cellulose 24 (11) (November 2017) 4743–4757.
[32] Susanna Holappa, Katri S. Kontturi, Arto Salminen, Jukka Seppälä, Janne Laine, Adsorption of hydrophobically end-capped poly(ethylene glycol) on cellulose, Langmuir 29 (45) (November 2013) 13750–13759.
[33] Dong Cheng, Yangbing Wen, Lijuan Wang, Xingye An, Xuhai Zhu, Yonghao Ni, Adsorption of polyethylene glycol (PEG) onto cellulose nano-crystals to improve its dispersity, Carbohydr. Polym. 123 (June 2015) 157–163.
[34] Lucas J. Andrew, Christopher M. Walters, Wadood Y. Hamad, Mark J. MacLachlan, Coassembly of cellulose nanocrystals and neutral polymers in iridescent chiral nematic films, Biomacromolecules 24 (2) (February 2023) 896–908.
[35] Vishnu Arumughan, Tiina Nypelö, Merima Hasani, Anette Larsson, Fundamental aspects of the non-covalent modification of cellulose via polymer adsorption, Adv. Colloid Interface Sci. 298 (December 2021) 102529.
[36] Christina Schütz, Michael Agthe, Andreas B. Fall, Korneliya Gordeyeva, Valentina Guccini, Michaela Salajková, Tomás S. Plivelic, Jan P.F. Lagerwall, German Salazar-Alvarez, Lennart Bergström, Rod packing in chiral nematic cellulose nanocrystal dispersions studied by small-angle X-ray scattering and laser diffraction, Langmuir 31 (23) (June 2015) 6507–6513.
[37] Jun Araki, Masahisa Wada, Shigenori Kuga, Steric stabilization of a cellulose microcrystal suspension by poly(ethylene glycol) grafting, Langmuir 17 (1) (January 2001) 21–27.
[38] Firas Azzam, Eder Siqueira, Sébastien Fort, Roumaïssa Hassaini, Frédéric Pignon, Christophe Travelet, Jean-Luc Putaux, Bruno Jean, Tunable aggregation and gelation of thermoresponsive suspensions of polymer-grafted cellulose nanocrystals, Biomacromolecules 17 (6) (June 2016) 2112–2119.
[39] Hugo Voisin, Adèle Vasse, Estelle Bonnin, Fabrice Cousin, Isabelle Capron, Tuning of the chiral nematic phase of cellulose nanocrystals by the adsorption of a short polymer on their surface, Cellulose 30 (13) (September 2023) 8299–8309.
[40] Qiyao Sun, Viviane Lutz-Bueno, Jiangtao Zhou, Ye Yuan, Peter Fischer, Polymer induced liquid crystal phase behavior of cellulose nanocrystal dispersions, Nanoscale Adv. 4 (22) (2022) 4863–4870.
[41] Maoqi Lin, Vikram Singh Raghuwanshi, Christine Browne, George P. Simon, Gil Garnier, Modulating the chiral nanoarchitecture of cellulose nanocrystals through interaction with salts and polymer, J. Colloid Interface Sci. 613 (May 2022) 207–217.
[42] Tonya Kuhl, Yuqing Guo, James L. Alderfer, Alan D. Berman, Deborah Leckband, Jacob Israelachvili, Sek Wen Hui, Direct measurement of polyethylene glycol induced depletion attraction between lipid bilayers, Langmuir 12 (12) (January 1996) 3003–3014.
[43] Derek Gray, Xiaoyue Mu, Chiral nematic structure of cellulose nanocrystal suspensions and films; polarized light and atomic force microscopy, Materials 8 (11) (November 2015) 7873–7888.
[44] Firas Azzam, Laurent Heux, Bruno Jean, Adjustment of the chiral nematic phase properties of cellulose nanocrystals by polymer grafting, Langmuir 32 (17) (May 2016) 4305–4312.
[45] Catherine D. Edgar, Derek G. Gray, Influence of dextran on the phase behavior of suspensions of cellulose nanocrystals, Macromolecules 35 (19) (September 2002) 7400–7406.
[46] Ze-Lian Zhang, Xiu Dong, Yi-Ning Fan, Lu-Ming Yang, Lu He, Fei Song, Xiu-Li Wang, Yu-Zhong Wang, Chameleon-inspired variable coloration enabled by a highly flexible photonic cellulose film, ACS Appl. Mater. Interfaces 12 (41) (October 2020) 46710–46718.
[47] Firas Azzam, Bruno Frka-Petesic, Enrico F. Semeraro, Fabrice Cousin, Bruno Jean, Small-angle neutron scattering reveals the structural details of thermosensitive polymer-grafted cellulose nanocrystal suspensions, Langmuir 36 (29) (July 2020) 8511–8519.
[48] Camila Honorato-Rios, Jan P.F. Lagerwall, Interrogating helical nanorod self-assembly with fractionated cellulose nanocrystal suspensions, Commun. Mater. 1 (1) (September 2020) 69.
[49] Thomas G. Parton, Richard M. Parker, Gea T. Van De Kerkhof, Aurimas Narkevicius, Johannes S. Haataja, Bruno Frka-Petesic, Silvia Vignolini, Chiral self-assembly of cellulose nanocrystals is driven by crystallite bundles, Nat. Commun. 13 (1) (May 2022) 2657.
[50] C.S. Mali, S.D. Chavan, K.S. Kanse, A.C. Kumbharkhane, S.C. Mehrotra, Dielectric relaxation of poly ethylene glycol-water mixtures using time domain technique, Indian J. Pure Appl. Phys. 45 (May 2007) 476–481.
[51] Stephen L. Brenner, V. Adrian Parsegian, A physical method for deriving the electrostatic interaction between rod-like polyions at all mutual angles, Biophys. J. (1974).
[52] Gustavo A. Carri, M. Muthukumar, Attractive interactions and phase transitions in solutions of similarly charged rod-like polyelectrolytes, J. Chem. Phys. 111 (4) (July 1999) 1765–1777.
[53] A. Stroobants, H. Lekkerkerker, T. Odijk, Effect of electrostatic interaction on the liquid crystal phase transition in solutions of rodlike polyelectrolytes, Macromolecules 19 (8) (1986) 2232–2238.
[54] L. Onsager, The effects of shape on the interaction of colloidal particles, Ann. N.Y. Acad. Sci. 51 (1949) 627–659.
[55] Greg van Anders, Daphne Klotsa, N. Khalid Ahmed, Michael Engel, Sharon C. Glotzer, Understanding shape entropy through local dense packing, Proc. Natl. Acad. Sci. 111 (45) (2014) E4812–E4821.
[56] W.J. Orts, L. Godbout, R.H. Marchessault, J.-F. Revol, Enhanced ordering of liquid crystalline suspensions of cellulose microfibrils: a small angle neutron scattering study, Macromolecules 31 (17) (August 1998) 5717–5725.
[57] David Attia, Neta Cohen, Guy Ochbaum, Yael Levi-Kalisman, Ronit Bitton, Rachel Yerushalmi-Rozen, Nano-to-meso structure of cellulose nanocrystal phases in ethylene–glycol–water mixtures, Soft Matter 16 (36) (2020) 8444–8452.
[58] Elina Niinivaara, Marco Faustini, Tekla Tammelin, Eero Kontturi, Water vapor uptake of ultrathin films of biologically derived nanocrystals: quantitative assessment with quartz crystal microbalance and spectroscopic ellipsometry, Langmuir 31 (44) (November 2015) 12170–12176.
[59] Sadaf Shafiei-Sabet, Wadood Y. Hamad, Savvas G. Hatzikiriakos, Rheology of nanocrystalline cellulose aqueous suspensions, Langmuir 28 (49) (December 2012) 17124–17133.